Control of Magnetopause Flux Rope Topology by Non-local Reconnection

Lars Mejnertsen[1]*, Jonathan P. Eastwood[1] and Jeremy P. Chittenden[2]

[1]Space and Atmospheric Physics Group, Blackett Laboratory, Imperial College London, London, United Kingdom, [2]Plasma Physics Group, Blackett Laboratory, Imperial College London, London, United Kingdom

Dayside magnetic reconnection between the interplanetary magnetic field and the Earth's magnetic field is the primary mechanism enabling mass and energy entry into the magnetosphere. During favorable solar wind conditions, multiple reconnection X-lines can form on the dayside magnetopause, potentially forming flux ropes. These flux ropes move tailward, but their evolution and fate in the tail is not fully understood. Whilst flux ropes may constitute a class of flux transfer events, the extent to which they add flux to the tail depends on their topology, which can only be measured *in situ* by satellites providing local observations. Global simulations allow the entire magnetospheric system to be captured at an instant in time, and thus reveal the interconnection between different plasma regions and dynamics on large scales. Using the Gorgon MHD code, we analyze the formation and evolution of flux ropes on the dayside magnetopause during a simulation of a real solar wind event. With a relatively strong solar wind dynamic pressure and southward interplanetary magnetic field, the dayside region becomes very dynamic with evidence of multiple reconnection events. The resulting flux ropes transit around the flank of the magnetosphere before eventually dissipating due to non-local reconnection. This shows that non-local effects may be important in controlling the topology of flux ropes and is a complicating factor in attempts to establish the overall contribution that flux ropes make in the general circulation of magnetic flux through the magnetosphere.

Keywords: flux rope, reconnection, flux transfer events, magnetosphere (magnetospheric configuration and dynamics), global modelling

INTRODUCTION

Magnetic reconnection is an important process in driving the dynamics of the Earth's magnetosphere (*e.g.* Eastwood et al., 2017 and references therein). When the interplanetary magnetic field (IMF) is southward (IMF $B_z < 0$), it allows for enhanced plasma entry into the magnetosphere by opening up magnetic field lines on the dayside and closing on the nightside (Dungey, 1961). In reality, reconnection is inherently three-dimensional and non-steady (Fu et al., 2015; Wang et al., 2020), causing the formation of Flux Transfer Events (FTEs). They are thought to transfer magnetic flux and hence energy into the magnetosphere when they are "open": connected to either of the planet's poles and to the IMF. Though the origin and evolution of FTEs are not fully understood, they have been observed to have a significant effect on magnetospheric dynamics and space weather.

FTEs are identified in spacecraft observations by their characteristic bipolar signature in magnetic field data, typically in the component normal to the magnetopause surface (Farrugia et al., 2016; Russell & Elphic, 1978). This signature may be indicative of rotational magnetic field structures called

flux ropes. While flux ropes exist in a variety of locations, such as on the solar surface or within coronal mass ejections, FTEs are specifically flux ropes generated on at the Earth's magnetopause, and range from $0.6R_E$ to $4.4R_E$ in size (Fear et al., 2007) They consist of twisted magnetic field structures which can persist due to their force-free nature. Furthermore, they typically contain plasma features due to reconnection (hot and high velocity plasma populations), variation in the magnetic field strength (Fear et al., 2008; Paschmann et al., 1982), and force-free magnetic fields (Farrugia et al., 2016).

With the majority of FTEs observed on the dayside, little is known about their transition around the magnetosphere. The prevailing theory is that once reconnection forms an FTE, it is accelerated along the magnetopause surface towards the cusps by the $\vec{J} \times \vec{B}$ force (Fedder et al., 2002; Russell & Elphic, 1978). However, FTEs have been observed far into the magnetotail ($x \simeq 67\ R_E$), where their axis has been rotated from aligned in the azimuthal direction (parallel to the $x_{GSE} - y_{GSE}$ plane) to aligned with the z_{GSE} axis (Eastwood et al., 2012).

One of the main difficulties in understanding FTEs and their impact is due to the relative sparseness of spacecraft observations. Multi-spacecraft missions such as the Magnetospheric Multiscale Mission (MMS), Time History of Events and Macro-scale Interactions during Substorms (THEMIS), and Cluster have improved our understanding of FTE size and motion (Farrugia et al., 2016; Fear et al., 2005, Fear et al., 2008). In an FTE observed by MMS, it was found that there were two distinct electron populations within the FTE: one characteristic of originating from the magnetosphere, and the other from the magnetosheath, suggesting a single FTE can have a complex magnetic topology (Kacem et al., 2018). Whilst auroral signatures of FTEs have been observed, they are rarely accompanied with a spacecraft in the correct position to observe the FTE structure. Hence, global simulations of the magnetosphere, which capture the magnetosphere as a whole, can be very useful in understanding a number of FTE features, giving insights into their formation, evolution, topology and impact on the magnetosphere.

A number of papers have used global simulations to study FTEs and flux ropes. Though it is known that MHD cannot capture the full physics required for reconnection, it has been shown that global simulations do capture the location of reconnection at the dayside magnetopause relatively well (Komar et al., 2015). Raeder (2006) used OpenGGCM to investigate the effect of dipole tilt on the generation of FTEs. Under a strongly southward IMF, the FTEs were formed by multiple x-line reconnection, and was modulated by the dipole tilt. Cardoso et al. (2013)'s simulation of a steady, strong South- and duskward IMF, found elbow-shaped flux tubes. Other flux tubes were found to be interlinked with field lines of different topology. Perez et al. (2018) further reported a study showing a number of flux ropes spontaneously forming under constant solar wind parameters.

The majority of simulations studying this problem have used idealized solar wind events, with inflow parameters usually kept constant. In this article, the Gorgon code (Ciardi et al., 2007;

Mejnertsen et al., 2016, 2018) is used to simulate flux ropes that are formed in response to a real interval of strongly southward IMF solar wind as observed by ACE and Cluster on March 31, 2001 (Maksimovic et al., 2003). By using a global simulation approach, the full three-dimensional structure of different flux ropes are found as a function of time. This allows their properties to be established, and their generation, transport and fate to be studied. Furthermore, their magnetic topology can be calculated, from which the amount of flux transferred into the magnetosphere can be inferred. The manuscript is organized as follows. In *Methodology*, we discuss the methodology, including the Gorgon MHD code and the properties of the solar wind on the day of interest. *Overview of the Event Simulation* provides an overview of the Simulation, and *Identification of Flux Ropes Through Field Line Tracing and Topology Mapping* describes in detail the methodology used to identify and study flux ropes at the magnetopause. *Results* presents the results of the flux rope analysis, and conclusions are summarized in *Conclusion*.

METHODOLOGY

The Gorgon MHD Code

In this work, we simulate the magnetosphere using the Gorgon 3D magnetohydrodynamic code. Gorgon was initially developed for studying high energy, collisional plasma interactions such as Z-pinches (Chittenden et al., 2004; Jennings, 2006; Jennings et al., 2010), laser-plasma interactions (Smith et al., 2007) and magnetic tower jets (Ciardi et al., 2007), but has recently been adapted to simulate planetary magnetospheres and their interaction with the solar wind (Desai et al., 2021; Eggington et al., 2020; Mejnertsen et al., 2016, 2018).

Gorgon uses a fully explicit, Eulerian formulation of the resistive MHD equations for a fully ionized hydrogen plasma, as given by **Equations 1 to 6**:

$$\frac{\partial \rho}{\partial t} + \vec{\nabla} \cdot \left(\rho \vec{v} \right) = 0, \tag{1}$$

$$\frac{\partial}{\partial t} \rho \vec{v} + \left(\vec{v} \cdot \vec{\nabla} \right) \rho \vec{v} = -\vec{\nabla} \left(P_e + P_p \right) + \vec{J} \times \vec{B}, \tag{2}$$

$$\frac{\partial \varepsilon_p}{\partial t} + \vec{\nabla} \cdot \left(\varepsilon_p \vec{v} \right) = -P_p \vec{\nabla} \cdot \vec{v} - \Delta_{pe}, \tag{3}$$

$$\frac{\partial \varepsilon_e}{\partial t} + \vec{\nabla} \cdot \left(\varepsilon_e \vec{v} \right) = -P_e \vec{\nabla} \cdot \vec{v} + \eta \left| \vec{J} \right|^2 - \Lambda + \Delta_{pe}, \tag{4}$$

$$\frac{\partial^2 \vec{A}}{\partial t^2} = -c^2 \vec{\nabla} \times \vec{\nabla} \times \vec{A} + \frac{\vec{J}}{\epsilon_0}, \tag{5}$$

$$\text{where } \eta \vec{J} = -\frac{\partial \vec{A}}{\partial t} + \vec{v} \times \vec{B}. \tag{6}$$

These equations describe the conservation of mass (1), momentum (2), proton energy (3), electron energy (4), the magnetic induction equation (5) and Ohms law (6), where ρ is the mass density, $\vec{v}$ is the bulk plasma flow, $P_{p,e}$ is the proton and electron pressure, $\vec{J}$ is the current density, $\vec{B}$ is the magnetic field, $\varepsilon_{p,e}$ is the ion and electron energy density and η is the plasma resistivity.
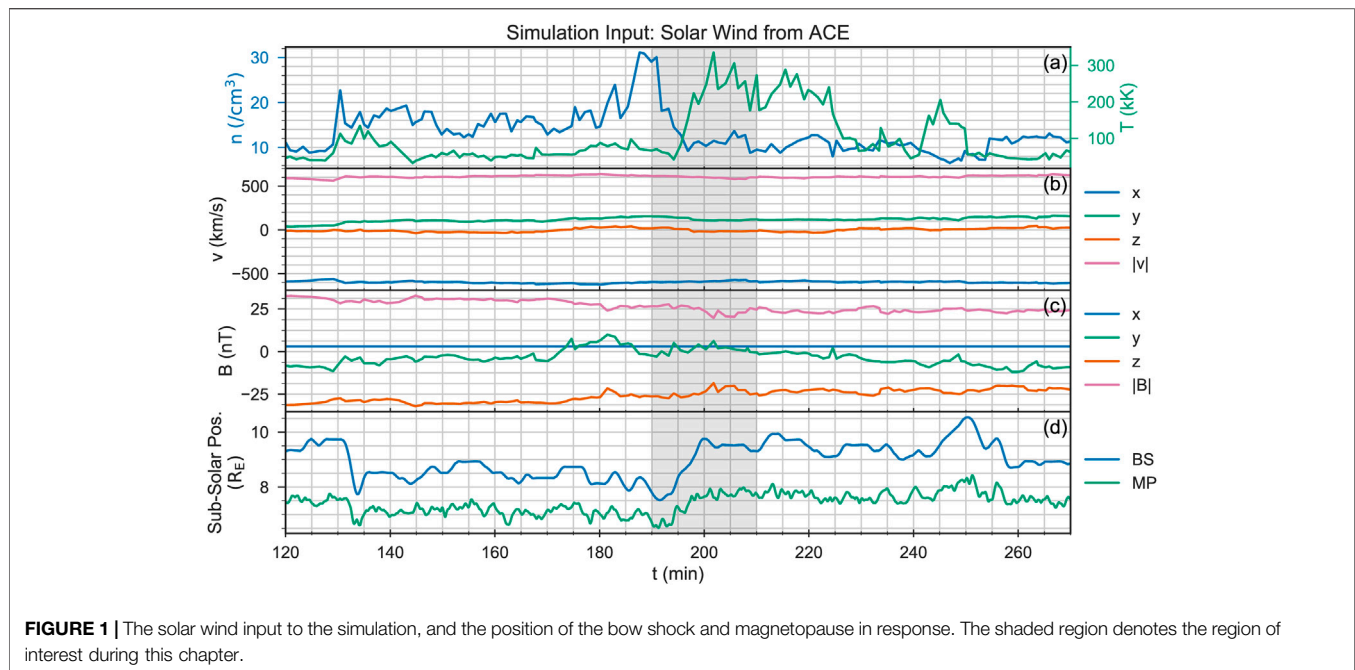
FIGURE 1 | The solar wind input to the simulation, and the position of the bow shock and magnetopause in response. The shaded region denotes the region of interest during this chapter.

Because of its roots in high energy plasma physics, the MHD formulation in Gorgon is atypical. Firstly, it treats the electron and proton energy equations separately (**Equations 3, 4**), allowing them to be out of thermodynamic equilibrium. These equations include terms for Ohmic heating $\eta|\vec{J}|^2$, optically thin radiation losses Λ, and electron-proton energy exchange Δ_{pe}. In the parameter regime of magnetospheric space plasmas, these terms are negligible, and hence have been disabled in the code or are also negligibly small. The pressure is calculated using the ideal gas law, with $\gamma = 5/3$. It makes use of second Order Van Leer advection to solve the advection terms in **Equations 1-6**. It also employs a variable timestep which automatically satisfies the relevant Courant conditions.

Secondly, the magnetic field solver uses the vector potential representation of the magnetic field, on a staggered grid (Yee, 1966). This allows the magnetic divergence condition to be satisfied automatically to machine accuracy, without using divergence cleaning algorithms. It also allows the electromagnetic fields to propagate through a vacuum. In the code, a vacuum is defined by a threshold density, below which plasma properties forces are set to zero. Here, the fields propagate as vacuum solutions to Maxwell's Equations.

Space plasmas are in general collisionless, meaning they have a very small resistivity and a broad applicability of the "frozen-in" flux theorem. Under ideal MHD, a process such as reconnection should not occur, as the fields cannot disassociate from the plasma. In numerical simulations, there is a numerical resistivity which allows the magnetic field to reconnect. This is dependent on the size of the grid. Whilst Gorgon is a resistive MHD code, this resistivity has been set to the Spitzer resistivity, which is lower than the numerical resistivity. A common approach in reconnection studies in global MHD simulations is to apply an anomalous resistivity

(Komar et al., 2015), and has been found necessary when simulating substorms (Raeder et al., 2001). However, numerous simulations (Raeder, 2006; Cardoso et al., 2013; Perez et al., 2018) have shown that flux ropes can form with numerical resistivity, and anomalous resistivity has no impact on dayside reconnection (Raeder, 2006).

In this work, we use the same simulation as in Mejnertsen et al. (2018). We simulate a region spanning $x_{GSE} = (-50, 30)R_E$, $y_{GSE} = (-20, 20)R_E$ and $z_{GSE} = (-30, 30)R_E$, with a uniform grid resolution of $0.2\,R_E$. The solar wind is applied on the sunward boundary of simulation domain, with von-Neumann conditions on all other boundaries.

MARCH 31, 2001

The work in this article also uses the same solar wind parameters as in Mejnertsen et al. (2018), from March 31, 2001 17:14:00 – 19:34:00 UT. This interval was the subject of a case study by Maksimovic et al. (2003), who used four spacecraft Cluster observations to characterize the motion of the bow shock in response to variation in the solar wind inflow. Whereas Mejnertsen et al. (2018) focused on the motion of the outer boundaries over the whole 2 hour period, but reduced to the ecliptic and noon-midnight plane, in this chapter the focus is on the formation of FTEs over a shorter 20 min timeframe. For this, the full three-dimensional state of the simulation is sampled at 10 s intervals.

The full solar wind input to the simulation is shown in **Figure 1**. However, now the focus is on the analysis interval from $t = 190$ min to 210 min as is indicated by the grey shaded region. The start of the simulated period (t = 0) is 15:14:00 UTC,

and so this corresponds to 18:24:00 – 18:44:00 UTC. During this time, the solar wind number density drops from $30 \,/\mathrm{cm}^3$ to $10 \,/\mathrm{cm}^3$, as seen in panel (a). The solar wind speed stays constant at approximately $600 \,\mathrm{km/s}$ (panel b). However, there is a significant v_y component, averaging approximately $100 \,\mathrm{km/s}$. The strength of the IMF (panel 3) was larger than typical IMF strength, ranging between $20 \,\mathrm{nT}$ and $25 \,\mathrm{nT}$. The dominating IMF component is the B_z component, with B_z starting at approximately $-30 \,\mathrm{nT}$ and reducing in magnitude slightly near the end. During this interval, the B_y component drops to approximately zero. With a negligibly small constant B_x, the IMF is predominantly southward, with no dawn-dusk component. The final panel 4) shows the sub-solar magnetopause and bow shock positions, as calculated by the methods in Mejnertsen et al. (2018). As expected, the reduction of solar wind number density causes the magnetopause distance to increase, from approximately $6.5 \, R_E$ to $7.5 \, R_E$. This causes the bow shock position to also increase in distance. The magnetopause position is much more variable than the bow shock position (Mejnertsen et al., 2018).

OVERVIEW OF THE EVENT SIMULATION

We first discuss the overall dynamics of the magnetopause during the 20 min interval of interest. The plasma number density in the ecliptic plane is shown in **Figure 2** at 1.5 min intervals from $t = 190$ min to 206.5 min. The solar wind streaming in from the left of each subplot first passes through the bow shock, shown by the increase in mass density. It flows around the magnetopause, which corresponds to the sharp cut-off in mass density. The magnetopause and bow shock are approximately conical, but oriented at an angle to the Sun-Earth line: this is due to the significant v_y component in the solar wind. At $t = 190$ min (panel 1), the magnetopause appears relatively smooth: there are only a few small structures, indicated by the bulges in the sharp density cut-off corresponding to the magnetopause. At this time, the solar wind number density is also at its highest, leading to the bow shock and magnetopause being most compressed, with a relatively thin magnetosheath. As time increases, the solar wind number density decreases, as can be seen by the decreasing magnitude of the color bar scales. This increases the magnetopause and bow shock standoff distances, and increases the magnetosheath width, which is most easily seen by comparing panels 1, 4, 7 and 10. As the number density decreases, more coherent structure forms on the magnetopause. On the dawn side, $y_{GSE} < 0$, there is a rippling of the magnetopause surface (indicated by the white dotted ellipse on **Figure 2**) which persists throughout each panel in **Figure 2** with varying amplitude. On the dusk side, $y_{GSE} > 0$, distinct bulges in the plasma can be seen propagating down the flanks of the magnetopause; an example of one is shown in **Figure 2** by the white dotted ellipse. These bulges are much more sporadic and intermittent than on the dawn side. An example of these bulges can be seen at $t = 193$ min, at position $x = 5 \, R_E$, $y = 10 \, R_E$, which propagates along the magnetopause surface before disappearing in the tail.

This same variability in the structure of the magnetosphere can also be seen in the current density magnitude, as shown in **Figure 3**. The magnetopause current density magnitude is largest in the sub-solar region, and decreases down the flanks. Many of the structures seen in the number density (**Figure 2**) are also visible here. On the dawn side, the same oscillatory feature can be seen (indicated by the white dotted circle on **Figure 3**), as well as the bulges moving down the dusk-side flank. More structure can also be seen on the sub-solar magnetopause. For example, at $t = 194.5$ min (panel 4), the magnetopause current sheet exhibits local variations in current density strength.

Figure 2 and **Figure 3** show that there are dynamic processes occurring on the magnetopause surface, which propagate down the flanks of the magnetosphere. We now discuss these features in more detail, finding that they are in fact caused by flux ropes associated with magnetic reconnection on the dayside magnetopause. We now describe the methodology used to identify flux ropes in the simulation before examining their properties in more detail.

IDENTIFICATION OF FLUX ROPES THROUGH FIELD LINE TRACING AND TOPOLOGY MAPPING

In order to visualize magnetic field lines and understand the features of the magnetopause, in particular to identify flux ropes, streamlines are calculated from the magnetic field vector field. This is performed for two reasons. The first is to establish the existence of flux ropes based on identifying twisted field line structures, and the second is to examine flux rope topology. Flux ropes may be open (connected at one end to the ionosphere with the other end in the solar wind), closed (connected at both ends to either the ionosphere), or entirely contained within the solar wind.

The quality of stream-tracing is heavily dependent on its starting (seed) point. By under-sampling the magnetic field, visualizations can miss vital structure and dynamics. Ideally, there would be multiple seed points for every grid cell to ensure that every flux rope of interest is captured. In typical simulation grid sizes, this is computationally prohibitive. To render stream-tracing feasible, it is only performed in regions of interest, such as on the dayside or the nightside flank, as is shown in **Figure 4**.

Since global simulations provide the full three-dimensional path of field lines, their topology can be found by categorizing the field line according to their end point location. In cases where both ends of the field line reaches the outer boundary, the field line is said to be part of the IMF, and is colored red. When both ends of the field line touch the inner boundary, it is said to be closed, and is colored blue. Open field lines occur when one end connects to the inner boundary, and the other to the outer boundary. Open field lines are further classified by which pole they reach: North (magnetic South) is purple, and South (magnetic North) is green. The final type of field line identified by the algorithm are so-called incomplete field lines, where one or both ends do not reach a simulation boundary. Computationally, the stream-tracer assign a finite number of
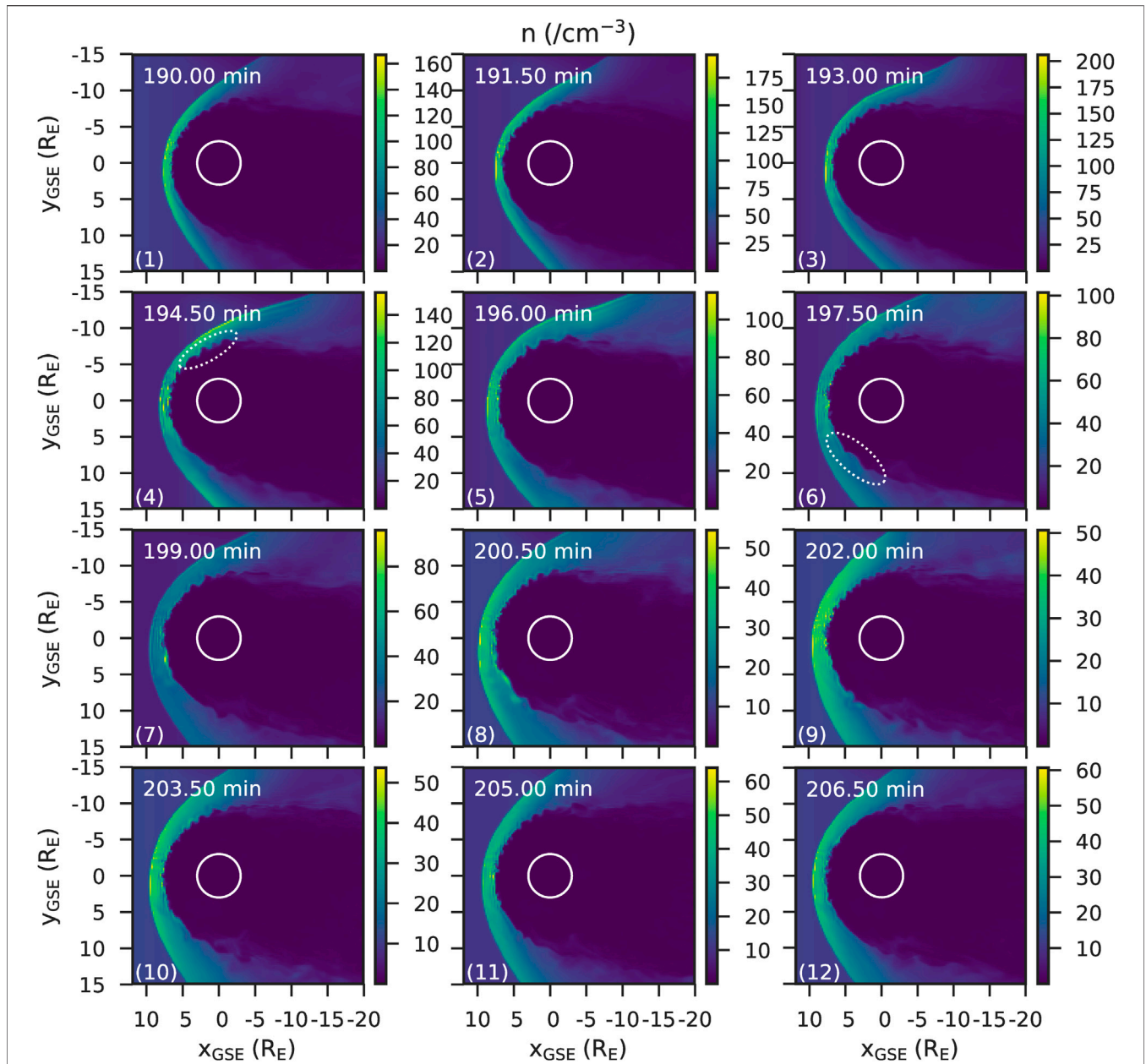
FIGURE 2 | The number density in the ecliptic plane every 1.5 min from t = 190 min to t = 206.5 min. The number density color bar scale changes every timestep. With the solar wind streaming from the left, the sharp increase in number density to the left denotes the bow shock. The brightly colored region after it is the magnetosheath. The subsequent sharp decrease moving to the right is the magnetopause. The white circle is the inner boundary of the simulation, of radius $3 R_E$.

steps to the streamline, so when the field line has not reached a boundary, it has likely run out of steps.

In order to filter out flux ropes from background magnetic field lines, the amount a field line twists or rotates is also computed. This measure of twist provides a way to isolate the twisted flux rope fields. The total rotation, Λ, is given by the angle between subsequent magnetic field directions along a field line,

$$\Lambda = \sum_i \cos^{-1}\left(-\hat{B}(s_i) \cdot \hat{B}(s_i + \Delta s)\right),$$

where s is the path along the field line and Δs is the stream-tracer step size. A perfectly straight field line will thus have $\Lambda = 0$. A perfectly circular field line will have $\Lambda = 2\pi = 360°$ after completing one revolution.
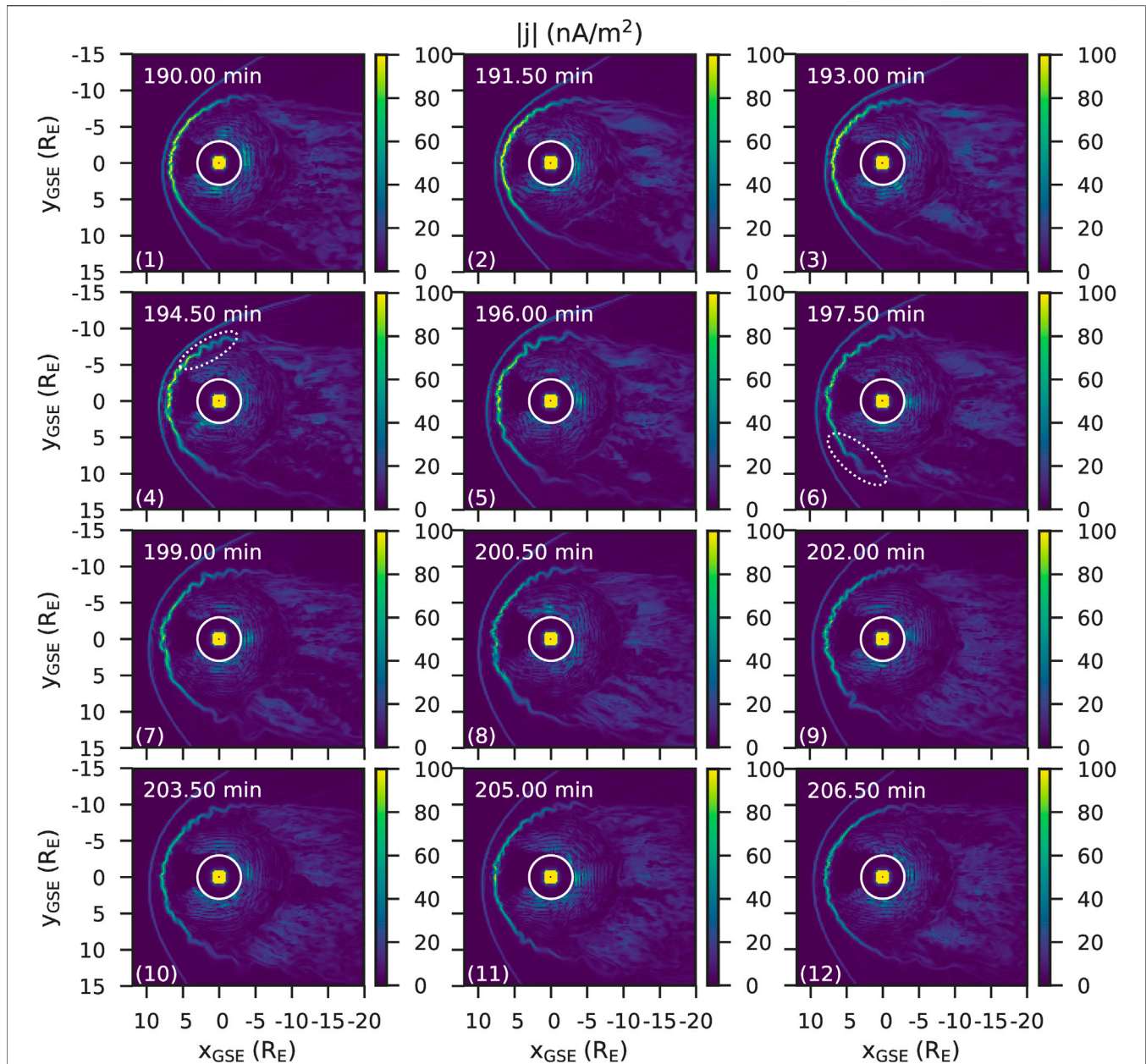
FIGURE 3 | The magnitude of the current density in the ecliptic plane every 1.5 min from **t** = 190 min to 206.5 min. As with **Figure 2**, the solar wind streams from the left. The compression of the magnetic field through the bow shock is shown as the left most current density peak. The magnetopause current sheet follows shortly after. Rather than a simple conical shape, it has oscillatory and transient structures. In the magnetotail, the white circle is the inner boundary of the simulation, of radius 3 R_E. The subsequent sharp decrease moving to the right is the magnetopause.

We note that the computation time can be decreased even further by removing the need to store every point in the field line and saving only the large-scale properties of each field line. This is used in topology mapping, where, for every seed point of interest, the field line is calculated to determine where it is connected to. An example of this is shown by the slice shown in **Figure 4**: a streamline is calculated from every position on that slice, and its topology is saved. This is then visualized on the slice.

By combining the topology mapping algorithm with calculations of the total rotation, Λ, regions where flux ropes have formed can be identified. Visualizing only field lines which exhibit flux rope characteristics gives a clearer picture of flux rope dynamics, whilst also finding all the flux ropes which meet the rotation criterion. The general method in plotting these flux ropes is as follows. For every timestep, the total rotation is calculated at cells in the simulation grid in the region of interest (e.g. the dayside). For each seed point where
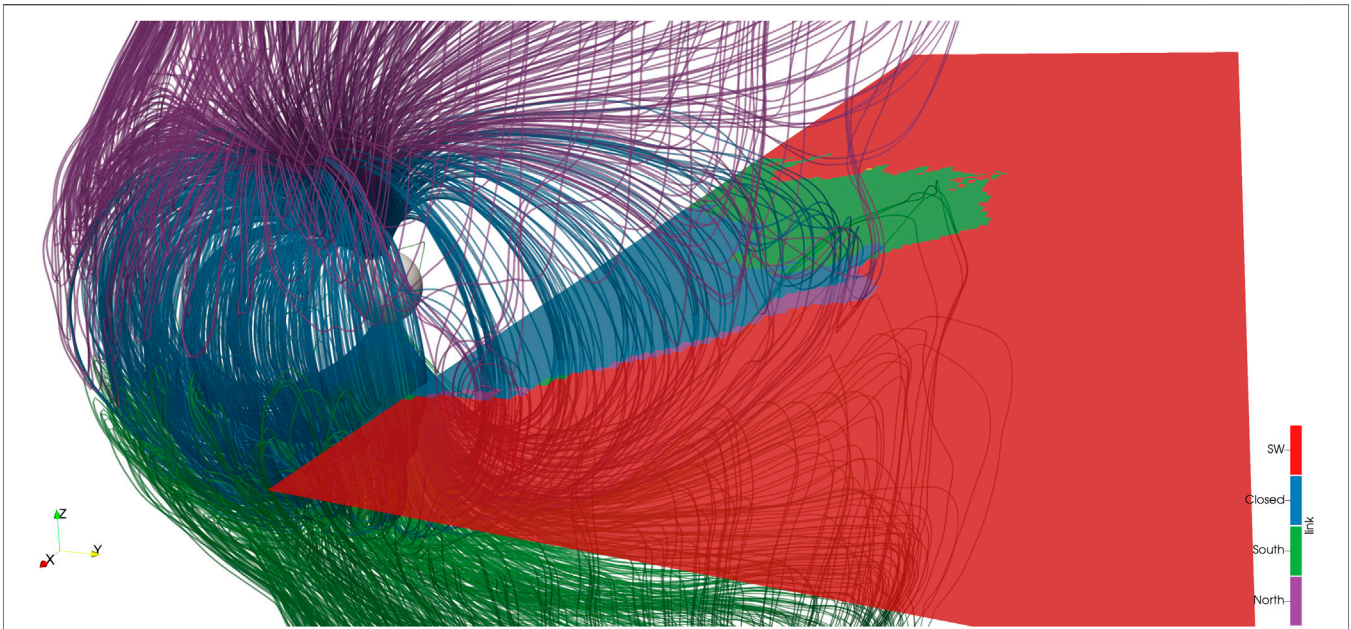
FIGURE 4 | An example of field line tracing and topology mapping. The magnetic field lines are colored by their topology: red for solar wind, blue for closed, green for open field lines connected to the South pole (magnetic North) and purple for open field lines connected to the North pole (magnetic South). The solar wind (red) field lines, which would dominate the view, have been filtered out. The slice shows the magnetic topology of cells along the ecliptic plane ($z_{GSE} = 0$): i.e. field lines connected to the red region are solar wind field lines, and map to the outer boundary of the simulation.
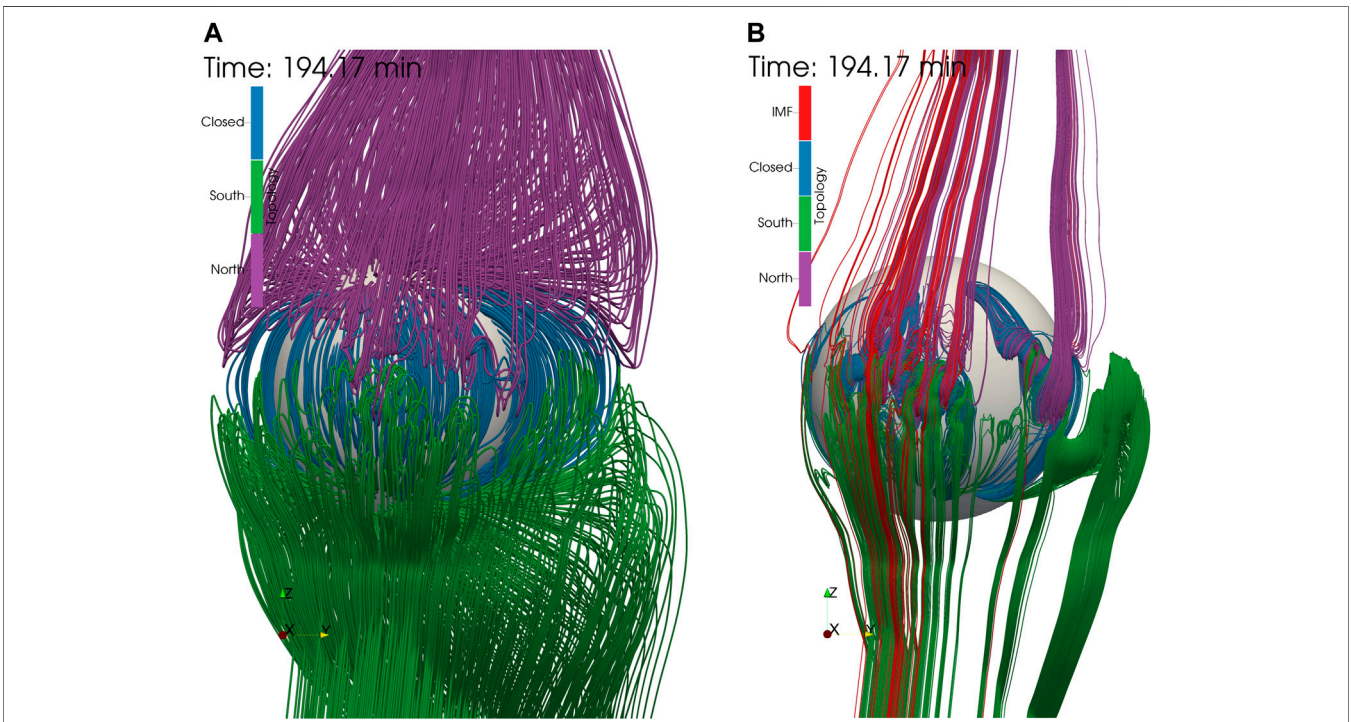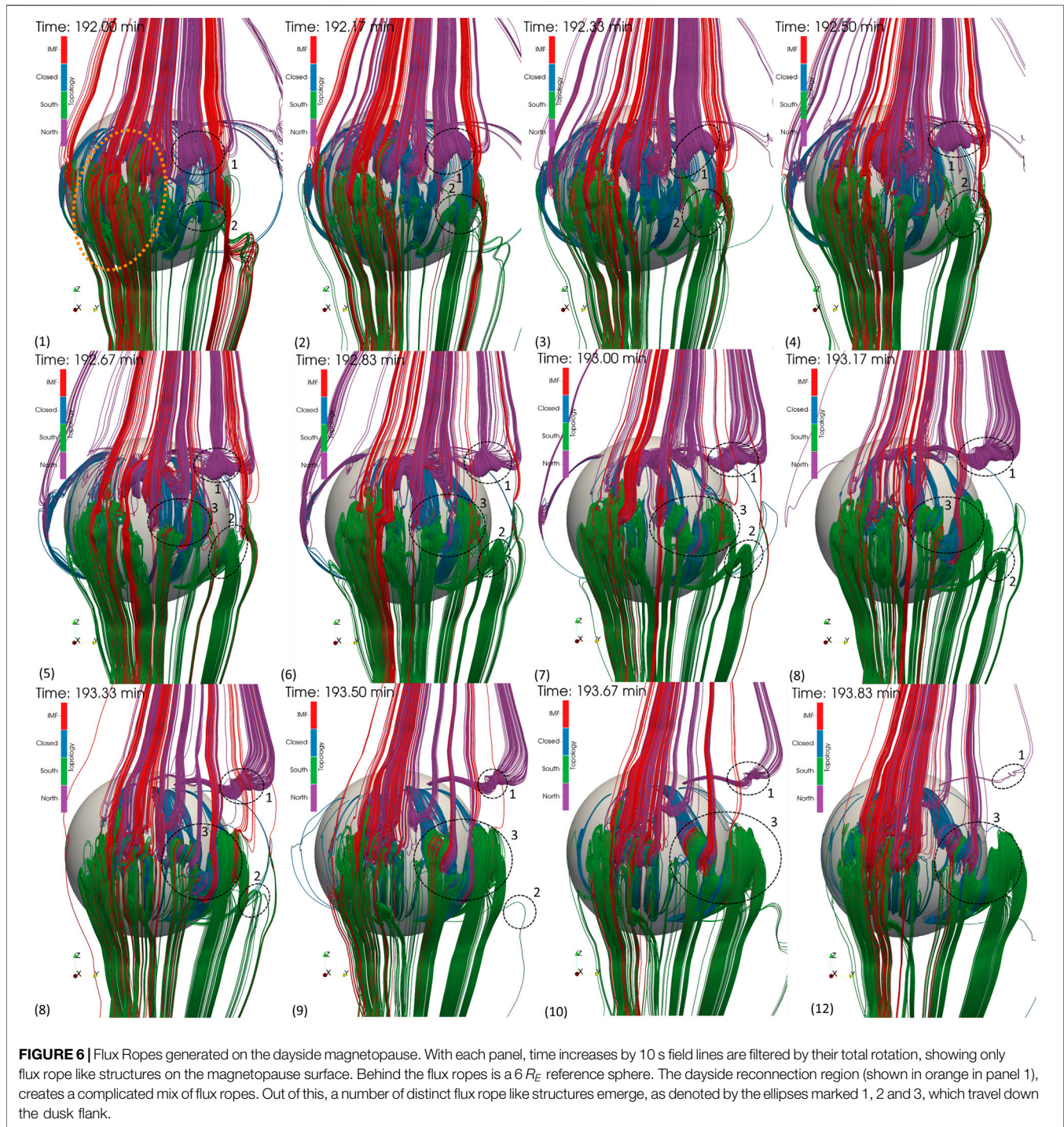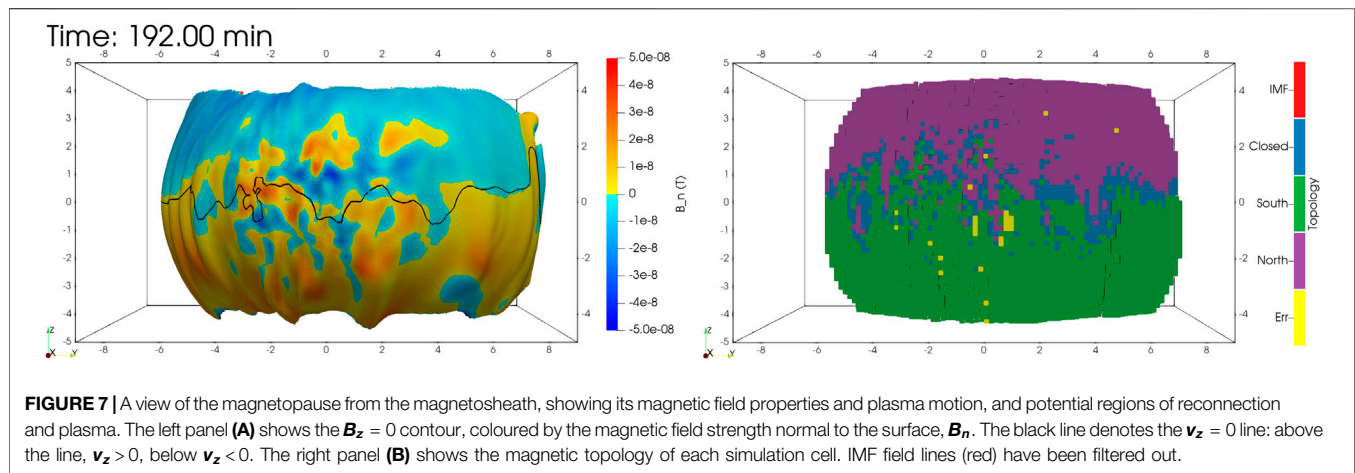

FIGURE 5 | By filtering field lines by rotation, flux rope structure can more easily be seen. Panel **(A)** shows field lines drawn from a regular spherical grid. Panel **(B)** shows field lines drawn from positions on the simulation grid with a high enough rotation, $\Lambda > 8\pi$.

FIGURE 6 | Flux Ropes generated on the dayside magnetopause. With each panel, time increases by 10 s field lines are filtered by their total rotation, showing only flux rope like structures on the magnetopause surface. Behind the flux ropes is a 6 R_E reference sphere. The dayside reconnection region (shown in orange in panel 1), creates a complicated mix of flux ropes. Out of this, a number of distinct flux rope like structures emerge, as denoted by the ellipses marked 1, 2 and 3, which travel down the dusk flank.

the Λ is large enough, usually $\Lambda > 8\pi$, their field line is drawn and its topology calculated. The threshold value of 8π was chosen through trial-and-error, as it allowed for effective filtering of non flux rope like field lines (e.g. draped field lines in the magnetosheath), whilst still including flux rope structures.

An illustration of the method is shown in **Figure 5**. In panel a, the field lines are drawn using seeds spread on a uniform spherical grid.

Whilst it does show some structure - for example, the magnetic separator can be inferred by the region separating the South (green) from the North (purple) field lines, it is difficult to see flux ropes, and the IMF has been filtered out as otherwise it would obscure the view of the magnetopause. In contrast, panel b shows the field lines filtered by the rotation method. Flux ropes can more easily be seen, and since the IMF field is not filtered out, examples of all four field topologies is visible.

FIGURE 7 | A view of the magnetopause from the magnetosheath, showing its magnetic field properties and plasma motion, and potential regions of reconnection and plasma. The left panel **(A)** shows the $B_z = 0$ contour, coloured by the magnetic field strength normal to the surface, B_n. The black line denotes the $v_z = 0$ line: above the line, $v_z > 0$, below $v_z < 0$. The right panel **(B)** shows the magnetic topology of each simulation cell. IMF field lines (red) have been filtered out.

RESULTS

Generation of Flux Ropes on the Dayside Magnetopause

Using the flux rope identification method described previously, **Figure 6** shows the existence of flux ropes on the dayside magnetopause during the interval of interest. As in *Identification of Flux Ropes Through Field Line Tracing and Topology Mapping*, magnetic field lines are colored by their topology: red for IMF, blue for closed, purple for open and connected to the North pole, and green for open and connected to the South pole. The reconnection region, approximately denoted by the orange ellipse in **Figure 6**, shows a complex entanglement of open, closed and IMF field lines, which can vary significantly over the 10 s time period. Out of the tangled reconnection region, distinct flux ropes propagate out along the magnetopause surface, predominantly along the dawn and dusk directions. They are generated with the flux rope axis parallel to the azimuthal direction, as is expected. These flux ropes start off relatively small, approximately $2\,R_E$ long in the azimuthal direction, and $\sim 1\,R_E$ wide.

From the first timestep at $t = 192$ min (panel **Figure 6**), two flux ropes have already formed (flux ropes 1 and 2), indicated by the black dashed ellipses. These are on opposite sides of the ecliptic plane: flux rope 1 is predominantly purple, indicating it is connected to the Northern pole, whilst flux rope two is predominantly green and is connected to the Southern pole. At $t > 192.33$ min (panels 1–3), both flux ropes are intertwined with closed field lines. This can best be seen in flux rope two in panel 2, which shows a blue strip wrapping around the green field lines. As time progresses, the closed field line region disappears, and the flux ropes move around the dusk flank toward higher latitudes.

At a later time $t = 192.67\,min$ (panel 5) a large-scale magnetic structure emerges from the dayside reconnection region, labelled as flux rope 3. This flux rope is complex in structure: it consists of a core of closed field lines (blue), around which open field lines are wrapped. The flux rope core magnetic field of closed magnetic field strength bends in a "U" shape, which is due to a velocity shear in the z direction which kinks the flux rope. Eventually, the "U" shape breaks, forming two flux ropes of different connectivity (**Figure 6**). As it travels toward the dusk flank, the South connected flux rope increases in azimuthal extent, whereas the North connected flux rope stays relatively small, and trails the South connected flux rope. Both flux ropes still have a core of closed magnetic field.
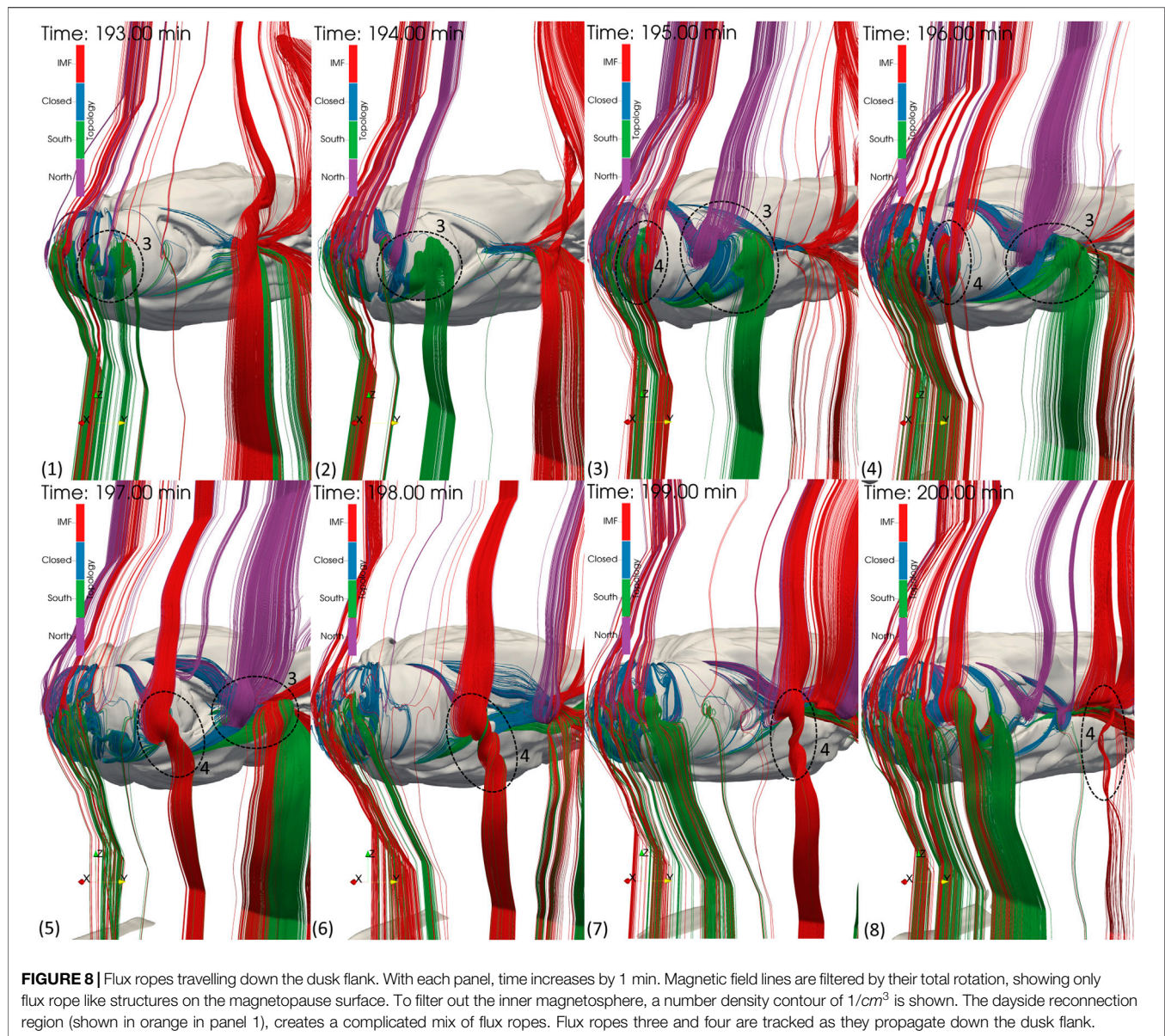
To make sense of the magnetopause reconnection region, the magnetopause surface is plotted in **Figure 7**. In panel (a), a three-dimensional iso-contour at $B_z = 0$ denotes the magnetopause surface. It is coloured by the magnetic field strength normal to the iso-contour surface, with the black line showing where $v_z = 0$. The $v_z = 0$ line is highly warped. Panel 2) shows the magnetic topology, filtering out the IMF field. Regions of closed field lines (blue) denotes places where reconnection could occur, since these have direct contact with the IMF. These regions tend to be clustered together in multiple lines, suggesting the multiple x-line reconnection is occurring.

Flux Rope Evolution

Figure 8 shows a three-dimensional view of the dusk flank of the magnetopause. Two flux ropes are tracked, flux ropes 3 and 4, which due to their differing topology evolve differently as they travel down the flanks.

Flux rope 3, first seen in **Figure 6**, moves down the flank for approximately 6 min until it begins to dissipate at $t \sim 198$ min between **Figure 8** and **Figure 8** reaches the tail reconnection region. As it travels down the flank, it increases in size along the flux rope axis. The axis of flux rope three for both North- and South-open sections remains parallel to the ecliptic plane throughout the simulation.

Flux rope four can be seen being generated in **Figure 8**, and contains a mix of all types of topology: closed, IMF, North- and South-open. Unlike flux rope 3, the two regions of opposite open topology do not separate, but remain as one flux rope. As flux rope four travels down the flank, its axis rotates from being in the ecliptic plane, to parallel to the z axis. It also increases in size along the flux rope axis. At the end, **Figure 8**, flux rope four is seen to only consist of IMF, and becomes less twisted.
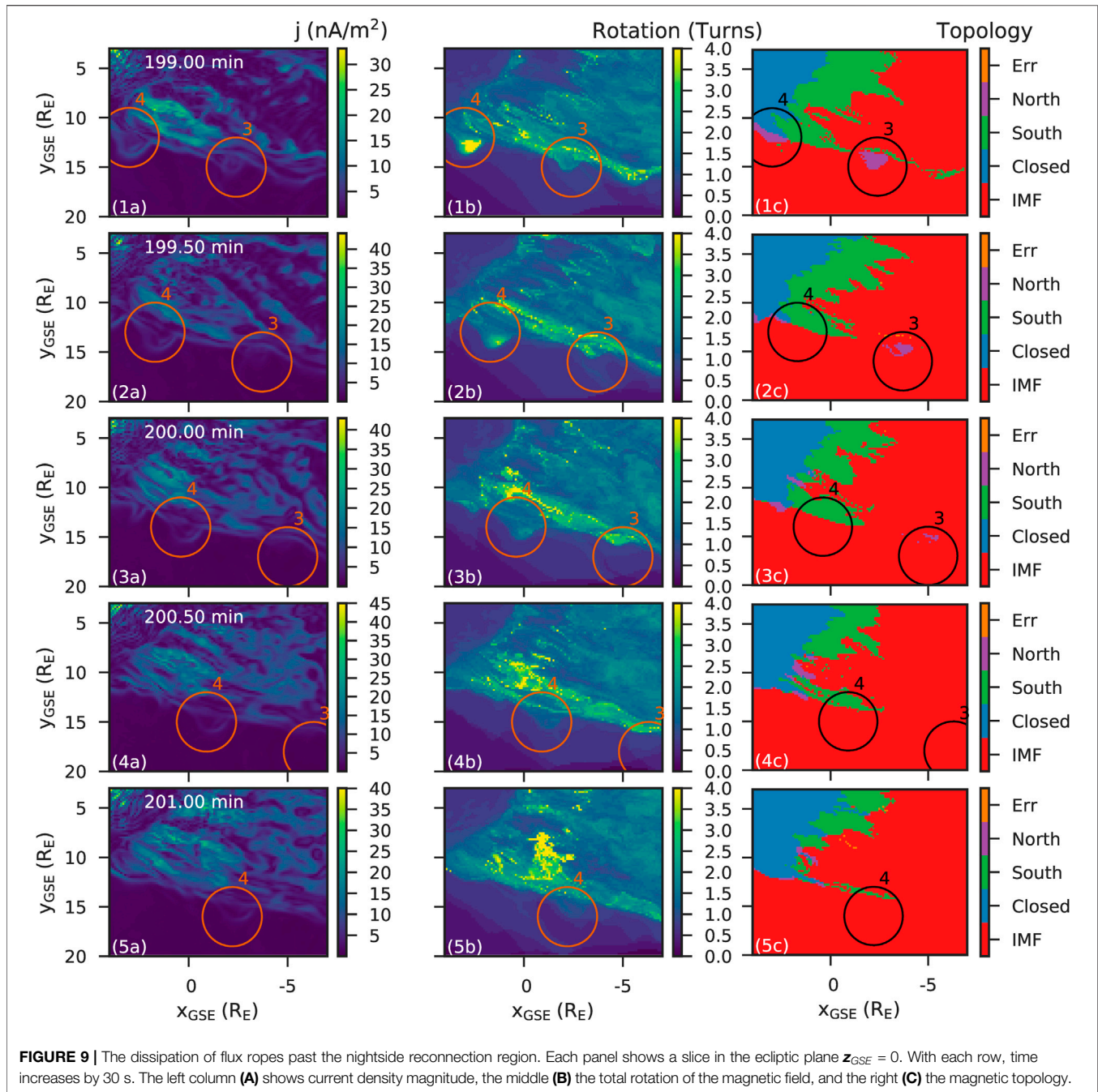
FIGURE 8 | Flux ropes travelling down the dusk flank. With each panel, time increases by 1 min. Magnetic field lines are filtered by their total rotation, showing only flux rope like structures on the magnetopause surface. To filter out the inner magnetosphere, a number density contour of $1/cm^3$ is shown. The dayside reconnection region (shown in orange in panel 1), creates a complicated mix of flux ropes. Flux ropes three and four are tracked as they propagate down the dusk flank.

Both flux ropes three and four behave differently as they travel down the flank due to their differing magnetic topology. However, both flux ropes dissipate shortly after reaching the nightside reconnection region. This can be seen in **Figure 9**, which shows slices of the simulation in the ecliptic plane as flux ropes three and four reach the tail reconnection region, with each row increasing in time by 30 s. The first column 1) shows current density magnitude, the middle 2) shows the total rotation of the magnetic field, and the right 3) shows the magnetic topology of the slice. In the topology plots (column c), the closed field line region can be seen by the blue region. The green region, connected to the South pole, essentially shows the tail reconnection region. The flank magnetopause is the region duskward of the blue and green regions, which coincides with

the current sheet shown in column (a). Flux ropes three and four are shown as islands of purple, North connected, magnetic field lines, marked with circles.

Row 1 shows flux rope four just approaching the tail reconnection region, where blue meets green (panel 1c). 30 s later, in row 2, the purple region has disappeared replaced by red. However, the flux rope is still there, as seen by the structure in the current (2a), as the high amount of rotation (2b). As time increases (rows three–5), flux rope four remains connected to the IMF, but continues to be twisted, as shown in column b be its enhanced total rotation. Its total rotation does decrease with time, suggesting the flux rope is unravelling.

A similar process occurs with flux rope 3, except that the open field line region persists long after the reconnection region. In the

FIGURE 9 | The dissipation of flux ropes past the nightside reconnection region. Each panel shows a slice in the ecliptic plane $z_{GSE} = 0$. With each row, time increases by 30 s. The left column **(A)** shows current density magnitude, the middle **(B)** the total rotation of the magnetic field, and the right **(C)** the magnetic topology.

first timestep shown in **Figure 9**, the purple, open field region has already passed the reconnection region. In subsequent time-steps, the purple region appears to dissipate, converting to red (IMF). This is due to the same reason as flux rope 4: reconnection occurs in the tail reconnection region, upstream of the flux rope rather than at the flux rope.

This process is shown in **Figure 10**. Viewing the dusk magnetotail from the $+x_{GSE}$, $+y_{GSE}$, $+z_{GSE}$ direction, the field lines from flux rope three are shown, as well as closed field lines near the Earth. These field lines have not been

filtered by total rotation. Flux rope three is manually tracked through the simulation and seed points chosen which encompass flux rope 3, denoted by the circles labelled three in **Figure 9**. In order to see the open field lines in the flux rope, the IMF field lines (red) start off transparent, but become opaque at $t = 200$ min when the flux rope contains no more open field lines. The closed field lines are generated from a grid in the $y_{GSE} - z_{GSE}$ plane, at $x = -5 R_E$, and only show the closed field lines (open and IMF field lines have been filtered out).
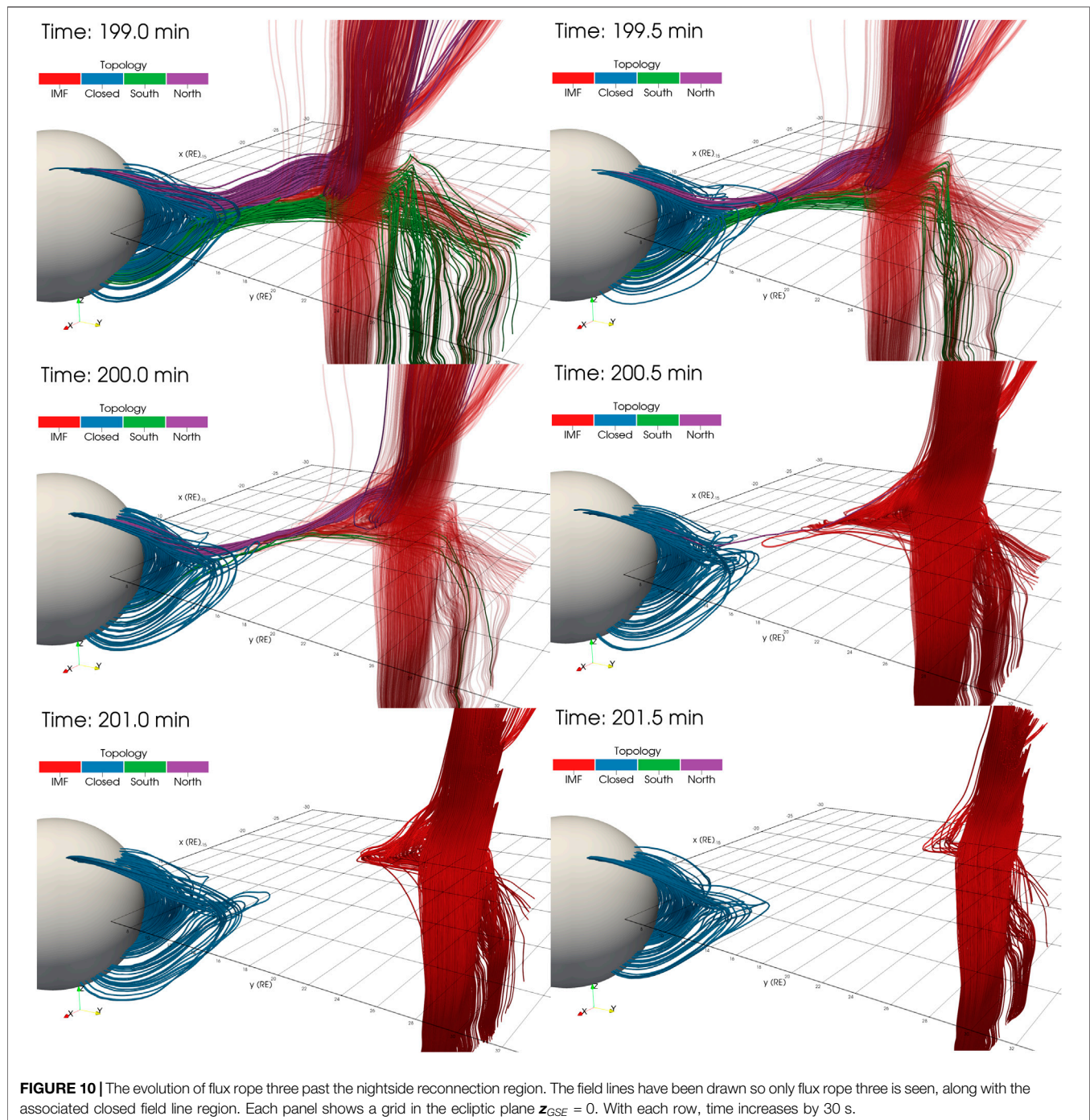
FIGURE 10 | The evolution of flux rope three past the nightside reconnection region. The field lines have been drawn so only flux rope three is seen, along with the associated closed field line region. Each panel shows a grid in the ecliptic plane $z_{GSE} = 0$. With each row, time increases by 30 s.

In **Figure 10**, two main field line regions are shown: the flux rope and the closed field line region. In between there are elongated field lines with a large B_x component, containing both open (green and purple), closed (blue) and IMF (red) field lines. As time progresses from $t = 199$ min to $t = 200.5$ min, the number of field lines in this region decreases, making the region thinner. At the same time, the amount of open field lines in the flux rope is decreasing. This

indicates that the flux rope is changing topology, reconnecting in between the flux rope and the closed field line region. This is supported in **Figure 9** which shows field line rotation (9.4b) but open topology (9.4c) at flux rope 3. At $t = 200.5$ min, the flux rope detaches completely from the planetary field, as is indicated by the now red field lines. These field lines still stretch from the flux rope, back to the reconnection site indicating the reconnection site occurred far from the actual flux rope.
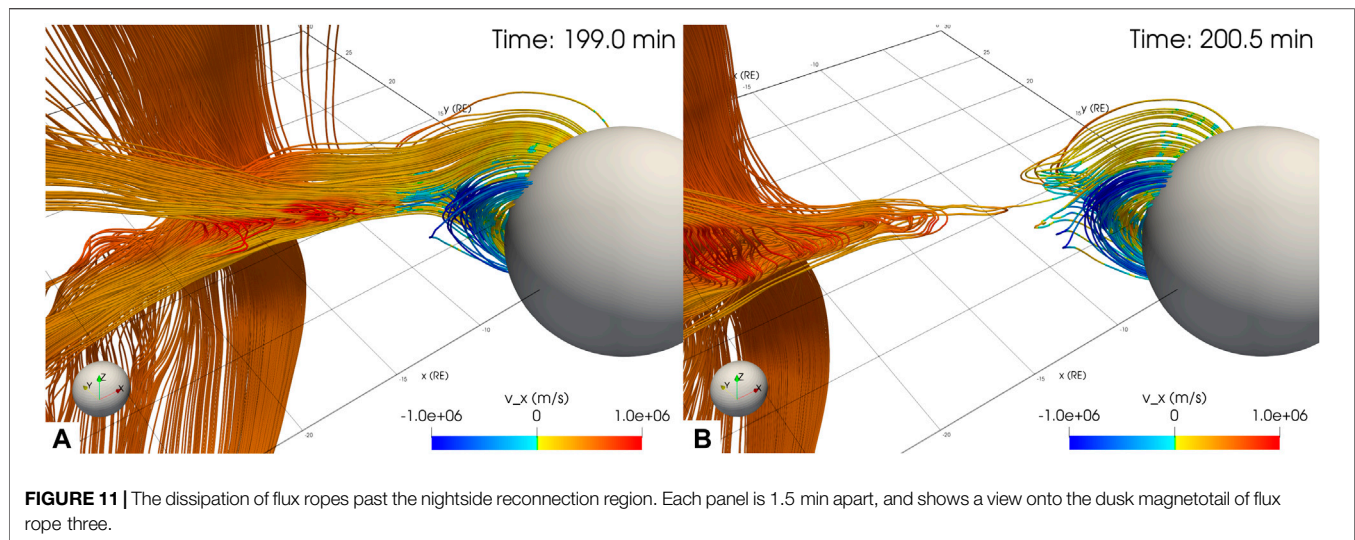
FIGURE 11 | The dissipation of flux ropes past the nightside reconnection region. Each panel is 1.5 min apart, and shows a view onto the dusk magnetotail of flux rope three.

Figure 11 shows the same field lines and sphere as **Figure 10**, except that they are colored by the plasma v_x and the view is onto dusk magnetotail from the $-x_{GSE}$, $-y_{GSE}$, $+z_{GSE}$. At the earlier time, $t = 199$ min, the flux rope is still attached to the planet. However, there is an enhanced v_x component in the $-x_{GSE}$ direction on the field lines in ellipse 1, and similarly, enhanced positive v_x on the closed field line region in ellipse 2. This suggests that reconnection is occurring, accelerating the plasma *via* the $\vec{J} \times \vec{B}$ force. At the later time, $t = 200.5$ min, the flux rope has completely reconnected, losing connectivity with the planet, with the same signature in v_x as the earlier time.

CONCLUSION

In this work, we have studied the evolution of flux ropes generated by a real solar wind event using the Gorgon global MHD simulation. The event, observed by Cluster on 2001-03-31, creates several flux ropes on the dayside, which propagate along magnetopause flanks. These flux ropes were identified using a novel magnetic field line filtering method based on computing their total rotation. While the method allowed for effective identification of tightly wound flux ropes, it may miss smaller flux ropes.

The flux ropes are formed on the dayside magnetopause surface, where the strongly southward IMF reconnects with the magnetospheric field. Overlapping the highly warped magnetopause current layer, there exists a complex interlaced set of field lines whose topologies vary from closed to open to completely IMF. This is due to time-dependent reconnection along multiple x-lines on the magnetopause. Out of this complex interwoven dayside field region emerge stand-alone flux ropes which propagate along the magnetopause surface. However, the latitude of their path is dependent on their topology. Flux ropes which are completely open - they are solely connected to a single pole (North/purple or South/green) - tend to move along the

magnetopause at high latitudes. These flux ropes would be the equivalent to the classic flux rope evolution picture where they move towards the cusps. No flux ropes were observed to go directly over the cusps.

Flux ropes containing both closed and open field lines connected to both the North and South poles were also generated on the dayside and remain along the ecliptic plane at low latitudes throughout their evolution. In the classic cusp flux rope picture, the $\vec{J} \times \vec{B}$ force acts to move the flux rope over the poles. Since this flux rope is connected to both poles, the two opposite curvature forces cancel out, carrying it along ecliptic plane in the direction of the magnetosheath plasma flow. The flux ropes were found to be force free, with the thermal pressure balancing the $\vec{J} \times \vec{B}$ force. These flux ropes move along the duskward flanks toward the tail, with their axis remaining parallel to the z direction as they move along the flank. However, once they move past the terminator, field lines present in the flux rope begin to reconnect non-locally in the nightside magnetotail current sheet. This alters the topology of the flux rope, detaching it from the magnetosphere. The flux rope-like structure then persists until unravelling ~1 min later.

This behavior is interesting because it shows that flux rope topology can change during its lifetime as a consequence of reconnection at locations far from the flux rope itself. It may also suggest that flux ropes on the flanks of the magnetopause may be more likely to be topologically disconnected from the ionosphere, (although this is tensioned against a possibly shorter lifetime). FTEs have previously been shown to create ionospheric signatures (e.g. Sandholt et al. (1986); Milan et al. (1999); Wild et al. (2001); Fear et al. (2009)), and so these ionospheric signatures may only partially represent the magnetopause dynamics, particularly away from the dayside. This behavior has further implications for the amount of flux that flux ropes transfer into the magnetosphere. Further work is required to establish how common these changes in topology are for different solar wind conditions, so as to better constrain the extent to which flux rope topologies observed on the dayside correspond to those subsequently found on the nightside.

In the simulated event, no flux ropes were found to transit along the dawnward flank. One potential reason for this is that the flux ropes on the dawnside magnetopause exhibit a total rotation of less than the threshold 8π, and were filtered out. The other reason could be due to the specific solar wind conditions, whose combination of solar wind and IMF parameters could predispose the flux ropes to transit along the duskward flanks. To fully determine the impact of solar wind and IMF parameters on the direction of transit, a thorough study of different solar wind conditions should be performed.Resistivity is an important aspect in simulating reconnection events and flux rope dynamics. In the Gorgon code, a low resistivity is inherent in the simulation due to numerical resistivity caused by the grid resolution. Previous studies of reconnection in Global MHD simulations have found that enhanced resistivity, either through coarse grid resolutions or an artificial resistivity, prevents the formation of FTEs and causes them to diffuse away rapidly (Komar et al., 2013; Raeder, 2006). With the introduction of an artificial resistivity in the Gorgon code, we would expect similar results with fewer flux ropes generated. Those that do generate are likely to dissipate due to resistive diffusion: this is likely unphysical due to the collisionless nature of magnetospheric plasmas.

One potentially fruitful avenue for future work may be to focus on comparing multi-spacecraft observations of flux ropes (e.g. MMS, THEMIS and Cluster) with global simulations using the same solar wind input, particularly where the local topology can be measured. This would allow the evolution of flux rope topology to be explored experimentally. These results may also be relevant for the SMILE mission, where imaging of the dayside magnetopause is expected to shed new light on the role of flux ropes and FTEs in global magnetospheric dynamics.

REFERENCES

Cardoso, F. R., Gonzalez, W. D., Sibeck, D. G., Kuznetsova, M., and Koga, D. (2013). Magnetopause Reconnection and Interlinked Flux Tubes. *Ann. Geophys.* 31 (10), 1853–1866. doi:10.5194/angeo-31-1853-2013

Chittenden, J. P., Lebedev, S. V., Jennings, C. A., Bland, S. N., and Ciardi, A. (2004). X-ray Generation Mechanisms in Three-Dimensional Simulations of Wire Array Z-Pinches. *Plasma Phys. Control Fusion* 46 (12B), B457–B476. doi:10.1088/0741-3335/46/12B/039

Ciardi, A., Lebedev, S. V., Frank, A., Blackman, E. G., Chittenden, J. P., Jennings, C. J., et al. (2007). The Evolution of Magnetic tower Jets in the Laboratory. *Phys. Plasmas* 14 (5), 056501. doi:10.1063/1.2436479

Desai, R. T., Freeman, M. P., Eastwood, J. P., Eggington, J. W. B., Archer, M. O., Shprits, Y. Y., et al. (2021). Interplanetary Shock-Induced Magnetopause Motion: Comparison between Theory and Global Magnetohydrodynamic Simulations. *Geophys. Res. Lett.* 48. doi:10.1029/2021GL092554

Dungey, J. W. (1961). Interplanetary Magnetic Field and the Auroral Zones. *Phys. Rev. Lett.* 6 (2), 47–48. doi:10.1103/PhysRevLett.6.47

Eastwood, J. P., Nakamura, R., Turc, L., Mejnertsen, L., and Hesse, M. (2017). The Scientific Foundations of Forecasting Magnetospheric Space Weather. *Space Sci. Rev.* 212 (3–4), 1221–1252. doi:10.1007/s11214-017-0399-8

Eastwood, J. P., Phan, T. D., Fear, R. C., Sibeck, D. G., Angelopoulos, V., Øieroset, M., et al. (2012). Survival of Flux Transfer Event (FTE) Flux Ropes Far along the Tail Magnetopause. *J. Geophys. Res.* 117 (A8), a–n. doi:10.1029/2012JA017722

Eggington, J. W. B., Eastwood, J. P., Mejnertsen, L., Desai, R. T., and Chittenden, J. P. (2020). Dipole Tilt Effect on Magnetopause Reconnection and the Steady-State Magnetosphere-Ionosphere System: Global MHD Simulations. *J. Geophys. Res. Space Phys.* 125 (7). doi:10.1029/2019JA027510

Farinas Perez, G., Cardoso, F. R., Sibeck, D., Gonzalez, W. D., Facskó, G., Coxon, J. C., et al. (2018). Generation Mechanism for Interlinked Flux Tubes on the Magnetopause. *J. Geophys. Res. Space Phys.* 123 (2), 1337–1355. doi:10.1002/2017JA024664

Farrugia, C. J., Lavraud, B., Torbert, R. B., Argall, M., Kacem, I., Yu, W., et al. (2016). Magnetospheric Multiscale Mission Observations and Non-force Free Modeling of a Flux Transfer Event Immersed in a Super-alfvénic Flow. *Geophys. Res. Lett.* 43 (12), 6070–6077. doi:10.1002/2016GL068758

Fear, R. C., Fazakerley, A. N., Owen, C. J., and Lucek, E. A. (2005). A Survey of Flux Transfer Events Observed by Cluster during Strongly Northward IMF. *Geophys. Res. Lett.* 32 (18), a–n. doi:10.1029/2005GL023811

Fear, R. C., Milan, S. E., Fazakerley, A. N., Fornaçon, K.-H., Carr, C. M., and Dandouras, I. (2009). Simultaneous Observations of Flux Transfer Events by THEMIS, Cluster, Double Star, and SuperDARN: Acceleration of FTEs. *J. Geophys. Res.* 114 (10), a–n. doi:10.1029/2009JA014310

Fear, R. C., Milan, S. E., Fazakerley, A. N., Lucek, E. A., Cowley, S. W. H., and Dandouras, I. (2008). The Azimuthal Extent of Three Flux Transfer Events. *Ann. Geophys.* 26 (8), 2353–2369. doi:10.5194/angeo-26-2353-2008

Fear, R. C., Milan, S. E., Fazakerley, A. N., Owen, C. J., Asikainen, T., Taylor, M. G. G. T., et al. (2007). Motion of Flux Transfer Events: a Test of the Cooling Model. *Ann. Geophys.* 25 (7), 1669–1690. doi:10.5194/angeo-25-1669-2007

Fedder, J. A., Slinker, S. P., Lyon, J. G., and Russell, C. T. (2002). Flux Transfer Events in Global Numerical Simulations of the Magnetosphere. *J. Geophys. Res.* 107 (A5), 1–11. doi:10.1029/2001JA000025

Fu, H. S., Vaivads, A., Khotyaintsev, Y. V., Olshevsky, V., André, M., Cao, J. B., et al. (2015). How to Find Magnetic Nulls and Reconstruct Field Topology with MMS Data?. *J. Geophys. Res. Space Phys.* 120 (5), 3758–3782. doi:10.1002/2015JA021082

Jennings, C. A., Cuneo, M. E., Waisman, E. M., Sinars, D. B., Ampleford, D. J., Bennett, G. R., et al. (2010). Simulations of the Implosion and Stagnation of

Compact Wire Arrays. *Phys. Plasmas* 17 (9), 092703. doi:10.1063/1.3474947

Jennings, C. A. (2006). *Radiation Transport Effects in Wire Array Z Pinches and Magneto-Hydrodynamic Modelling Techniques*. Doctoral dissertation. Imperial College London.

Kacem, I., Jacquey, C., Génot, V., Lavraud, B., Vernisse, Y., Marchaudon, A., et al. (2018). Magnetic Reconnection at a Thin Current Sheet Separating Two Interlaced Flux Tubes at the Earth's Magnetopause. *J. Geophys. Res. Space Phys.*, 1–15. doi:10.1002/2017JA024537

Kane Yee, K. (1966). Numerical Solution of Initial Boundary Value Problems Involving maxwell's Equations in Isotropic media. *IEEE Trans. Antennas Propagat.* 14 (3), 302–307. doi:10.1109/TAP.1966.1138693

Komar, C. M., Cassak, P. A., Dorelli, J. C., Glocer, A., and Kuznetsova, M. M. (2013). Tracing Magnetic Separators and Their Dependence on IMF Clock Angle in Global Magnetospheric Simulations. *J. Geophys. Res. Space Phys.* 118 (8), 4998–5007. doi:10.1002/jgra.50479

Komar, C. M., Fermo, R. L., and Cassak, P. A. (2015). Comparative Analysis of Dayside Magnetic Reconnection Models in Global Magnetosphere Simulations. *J. Geophys. Res. Space Phys.* 120 (1), 276–294. doi:10.1002/2014JA020587

Maksimovic, M., Bale, S. D., Horbury, T. S., and André, M. (2003). Bow Shock Motions Observed with CLUSTER. *Geophys. Res. Lett.* 30 (7), 41–46. doi:10.1029/2002GL016761

Mejnertsen, L., Eastwood, J. P., Chittenden, J. P., and Masters, A. (2016). Global MHD Simulations of Neptune's Magnetosphere. *J. Geophys. Res. Space Phys.* 121 (8), 7497–7513. doi:10.1002/2015JA022272

Mejnertsen, L., Eastwood, J. P., Hietala, H., Schwartz, S. J., and Chittenden, J. P. (2018). Global MHD Simulations of the Earth's Bow Shock Shape and Motion under Variable Solar Wind Conditions. *J. Geophys. Res. Space Phys.* 123 (1), 259–271. doi:10.1002/2017JA024690

Milan, S. E., Lester, M., Greenwald, R. A., and Sofko, G. (1999). The Ionospheric Signature of Transient Dayside Reconnection and the Associated Pulsed Convection Return Flow. *Ann. Geophys.* 17 (9), 1166–1171. doi:10.1007/s00585-999-1166-2

Paschmann, G., Haerendel, G., Papamastorakis, I., Sckopke, N., Bame, S. J., Gosling, J. T., et al. (1982). Plasma and Magnetic Field Characteristics of Magnetic Flux Transfer Events. *J. Geophys. Res.* 87 (A4), 2159. doi:10.1029/JA087iA04p02159

Raeder, J. (2006). Flux Transfer Events: 1. Generation Mechanism for strong Southward IMF. *Ann. Geophys.* 24 (1), 381–392. doi:10.5194/angeo-24-381-2006

Raeder, J., Wang, Y. L., Fuller-Rowell, T. J., and Singer, H. J. (2001). Global Simulation of Magnetospheric Space Weather Effects of the Bastille Day Storm. *Solar Phys.* 204 (1/2), 323–337. doi:10.1023/A:1014228230714

Russell, C. T., and Elphic, R. C. (1978). Initial ISEE Magnetometer Results: Magnetopause Observations. *Space Sci. Rev.* 22 (6), 681–715. doi:10.1007/BF00212619

Sandholt, P. E., Deehr, C. S., Egeland, A., Lybekk, B., Viereck, R., and Romick, G. J. (1986). Signatures in the Dayside aurora of Plasma Transfer from the Magnetosheath. *J. Geophys. Res.* 91 (A9), 10063. doi:10.1029/JA091iA09p10063

Smith, R. A., Lazarus, J., Hohenberger, M., Marocchino, A., Robinson, J. S., Chittenden, J. P., et al. (2007). High Resolution Imaging of Colliding Blast Waves in Cluster media. *Plasma Phys. Control Fusion* 49 (12B), B117–B124. doi:10.1088/0741-3335/49/12B/S11

Wang, Z., Fu, H. S., Vaivads, A., Burch, J. L., Yu, Y., and Cao, J. B. (2020). Monitoring the Spatio-Temporal Evolution of a Reconnection X-Line in Space. *ApJ* 899 (2), L34. doi:10.3847/2041-8213/abad2c

Wild, J. A., Cowley, S. W. H., Davies, J. A., Khan, H., Lester, M., Milan, S. E., et al. (2001). First Simultaneous Observations of Flux Transfer Events at the High-Latitude Magnetopause by the Cluster Spacecraft and Pulsed Radar Signatures in the Conjugate Ionosphere by the CUTLASS and EISCAT Radars. *Ann. Geophys.* 19 (10/12), 1491–1508. doi:10.5194/angeo-19-1491-2001